Role of gas molecule complexity in environmental electron microscopy and photoelectron yield spectroscopy

Toby W. Shanley, Fadi Bonnie, John Scott, and Milos Toth*

School of Physics and Advanced Materials, University of Technology, Sydney, Australia

E-mail: Milos.Toth@uts.edu.au

Abstract

Environmental scanning electron microscopy (ESEM) and environmental photoelectron yield spectroscopy (EPYS) enable electron imaging and spectroscopy of surfaces and interfaces in low vacuum, gaseous environments. The techniques are both appealing and limited by the range of gases that can be used to amplify electrons emitted from a sample, and used to form images/spectra. However, to date, only H_2O and NH_3 gases have been identified as highly favorable electron amplification media. Here we demonstrate that ethanol vapor (CH_3CH_2OH) is superior to both of these, and attribute its performance to molecular complexity and valence orbital structure. Our findings improve present understanding of what constitutes a favorable electron amplification gas, and will help expand the applicability and usefulness of the ESEM and EPYS techniques.

Introduction

Environmental scanning electron microscopy (ESEM) is a common tool for imaging of materials that charge up during electron irradiation and can not be studied using conventional, high vacuum microscopes.[1-3] Moreover, the use of a gaseous environment inside the specimen chamber enables SEM studies of vacuum-incompatible materials and processes. For example, H_2O vapor, the most common ESEM imaging gas, enables real-time nano and micro scale studies of water droplet formation and the wettability of surfaces,[4-8] nanoparticle self-assembly during condensation,[9] humidity-induced swelling,[10] water transport through carbon nanopipes,[11] chemical vapor deposition of nanowires in dry and wet environments,[12] beam-directed electrodeposition performed using aqueous deposition precursors,[13,14] and electron beam induced etching of carbonaceous materials.[15-19] The most attractive feature of ESEM is the ability to image these processes and materials in real time with SEM spatial resolution. However, the gas employed in ESEM plays a central role in secondary electron (SE) amplification (Figure 1a) and electron image quality, and the applicability of ESEM is limited by the fact that only a handful of gases have favorable electron amplification characteristics. Numerous potential ESEM imaging gases have been evaluated to date, including air, CO_2, N_2O, N_2, He and NH_3.[20,21] However, all of these except for NH_3 have been shown to be inferior SE amplification media relative to H_2O.

Environmental photoelectron yield spectroscopy (EPYS)[22-25] is an emerging surface analysis technique which is analogous to ESEM in that it permits the use of gaseous environments in conjunction with measurements that are typically performed only in high or ultra-high vacuum. EPYS exploits the photoelectron effect, and entails measurement of the photoelectron emission current as a function of the energy of incident photons. It enables characterization of the electronic properties of a surface as it is modified by gas-mediated (spontaneous or thermally driven) chemical reactions. However, as in the case of ESEM, the gas used in the EPYS analysis chamber is used to amplify the emitted electrons in a gas ionization cascade (Figure 1b and c), and therefore limits the signal-to-noise ratio of EPYS spectra and the

scope and applicability of the technique.

Here, we identify ethanol vapor (CH_3CH_2OH) as an excellent gas amplification medium for secondary electrons in ESEM and photoelectrons in EPYS. We show that ethanol is superior to H_2O and NH_3, the only two high performance electron amplification gases reported to date. The superior properties of CH_3CH_2OH can not be explained by standard ESEM gas selection guidelines which are based on the first ionization energy of the gas molecules. Instead, we ascribe it to the valence orbital structure of the molecules. This finding will help guide identification and selection of high performance gases and gas mixtures for ESEM and EPYS, and will enable broader deployment of these imaging and spectroscopic techniques. In particular, the use of ethanol and other complex gas molecules paves the way to real-time studies of processes such as chemical vapor deposition, wetting dynamics of organic nanodroplets, heterogeneous catalysis, and other gas-solid reactions using ESEM and EPYS.
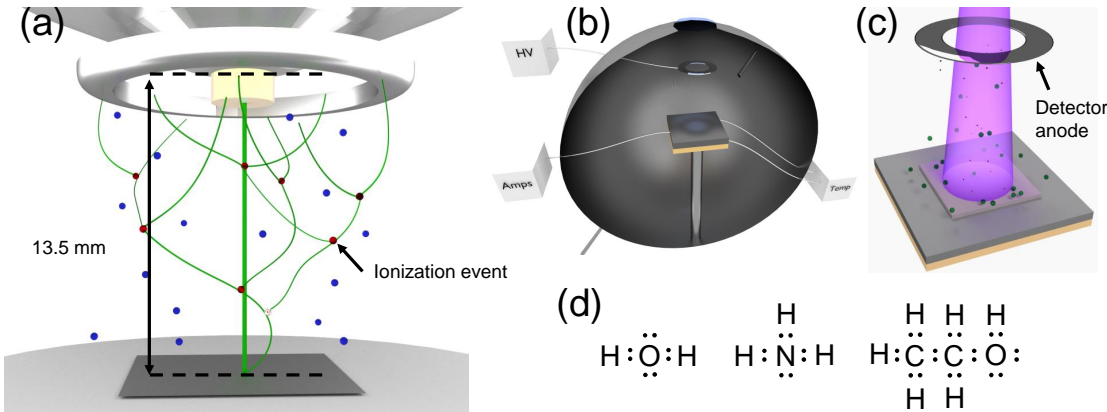

Figure 1: Schematic illustration of (a) electron amplification in an ESEM gas ionization cascade, (b) an EPYS vacuum chamber, and (c) photoelectron amplification in an EPYS gas ionization cascade. In both methods, electrons are accelerated by an electric field between the sample and a detector anode, and are amplified by ionizing gas molecules. Electrons and ions generated in the cascade flow to and away from the anode, respectively, and currents induced in the anode or the specimen stage can be used to form ESEM images and EPYS spectra. The EPYS chamber consists of a pumping system (not shown), gas inlet and outlet, specimen stage, heater, gas cascade detector, and an optical window. (d) Lewis diagrams showing the number of valence electrons contributing to the interaction cross sections of H_2O, NH_3 and CH_3CH_2OH.

Experimental Section

The ESEM gas cascade amplification efficiencies of H_2O, NH_3 and CH_3CH_2OH were evaluated by measuring the specimen stage current (see Figure 1a) versus gas pressure and detector anode bias using a variable pressure FEI XL-30 ESEM. The electron beam energy and current were fixed at 20 keV and 2.1 nA, and the sample-anode gap was 13.5 mm. A polycrystalline platinum foil sample and a Faraday cup were used to measure the total gas-amplified electron signal (I_Σ), and the component generated by gas cascade amplification of electrons liberated from gas molecules ionized by the electron beam, respectively. The difference between these two values is the gas-amplified electron emission current ($I_{\delta+\eta}$), generated by secondary and backscattered electrons emitted from the sample.

Complimentary EPYS measurements were performed using the same polycrystalline platinum foil sample, and the system that is shown in Figure 1 and has been described previously[25] (the EPYS sample-anode gap distance was 12 mm). Briefly, low energy photoelectrons were generated by illuminating the sample with broadband UV light spanning the spectral range of approximately 180-350 nm. The spot size had a diameter of ~5 mm. The EPYS technique has previously not been used for characterisation of gas cascade amplification. Our results demonstrate that such an analysis is highly complementary to ESEM studies which are complicated by the fact that high energy backscattered electrons are emitted from the sample and amplified by the ESEM imaging gas in parallel with SEs. This is problematic because the gas amplification characteristics of backscattered electrons are different from those of SEs, due to large differences between their energy spectra.[26,27] In contrast, the cascade-amplified EPYS current (I_p) has a single component generated by photoelectrons which are emitted over a narrow band of energy ($0 < E < 7$ eV) that is similar to the energy spectrum of SEs in ESEM (SE imaging is the most common SEM/ESEM imaging mode because it yields high resolution topographic contrast and electronic structure contrast[3,28–32]).

We note that deposition of carbon was not observed during the ESEM and EPYS experi-
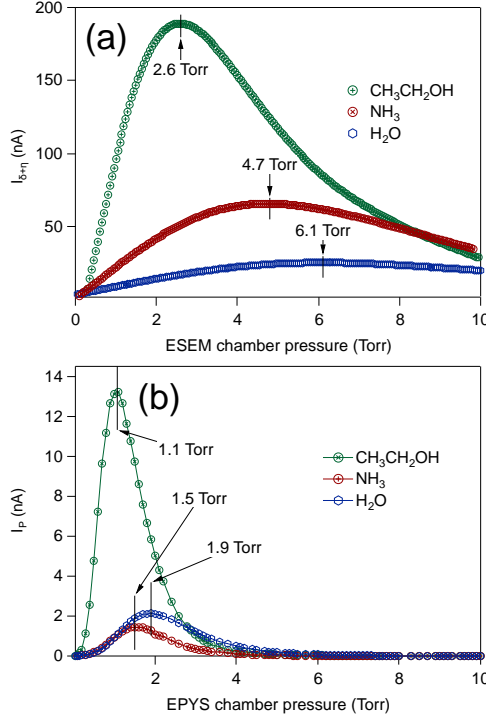
Figure 2: Gas-amplified electron emission current measured versus pressure using ethanol, NH_3 and H_2O. (a) In ESEM, the current is a sum of two components ($I_{\delta+\eta}$) that correspond to cascade-amplified, low energy (≤ 20 eV) secondary electrons and high energy (≤ 20 keV) backscattered electrons. (b) In EPYS the current (I_p) is generated by low energy (< 7 eV) photoelectrons. The detector anode bias was fixed at 400 V in both cases.

ments. Consequently, all results were reproducible when repeat acquisitions were performed using fixed sample regions. The absence of deposition in an ethanol atmosphere is attributed to negligible coverage of ethanol adsorbates at room temperature.

Results and Discussion

Figure 2(a) shows plots of $I_{\delta+\eta}$ versus pressure, measured for ethanol, NH_3 and H_2O using an ESEM. Ethanol is the most efficient amplifier over the entire pressure range typically used in ESEM (< 6 Torr). Optimum amplification in ethanol, NH_3 and H_2O occurs at 2.6, 4.7 and 6 Torr respectively.

Figure 2b shows equivalent EPYS data, revealing the same trend for gas-amplified pho-toelectrons. Ethanol is the most efficient amplifier at pressures smaller than ~ 2.5 Torr, and

optimum amplification in ethanol, NH_3 and H_2O occurs at 1, 1.5 and 1.9 Torr respectively. The differences between the ESEM and EPYS data (i.e. the EPYS curves are shifted to lower pressures) arises from the contribution of backscattered electrons to the ESEM signal. Backscattered electrons have significantly higher energy than secondaries, and optimal amplification therefore occurs at higher pressures.[26,27,33]
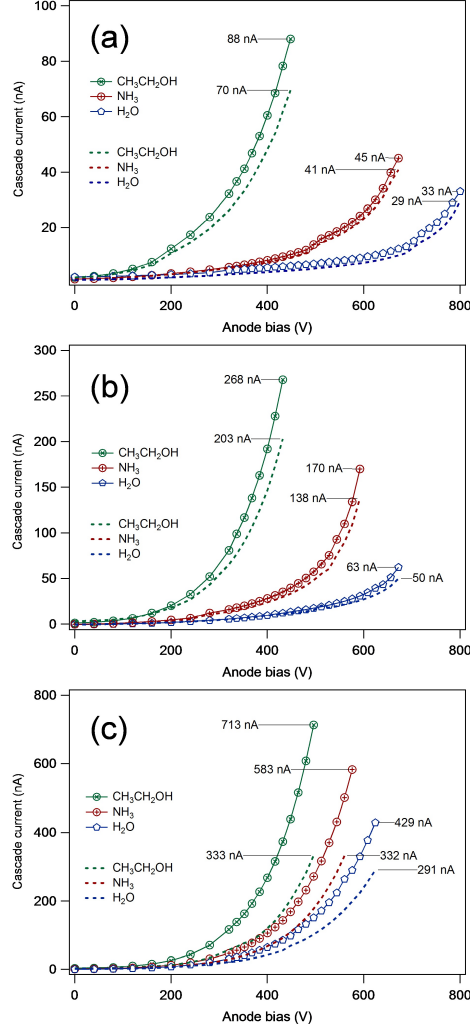

Figure 3: Total gas-amplified electron signal (I_Σ) and the gas-amplified electron emission current ($I_{\delta+\eta}$) measured versus ESEM detector anode bias using ethanol, NH_3 and H_2O, at gas pressures of (a) 0.1 Torr, (b) 1 Torr, and (c) 5 Torr. The maximum current reached at the onset of dielectric breakdown of the gas is shown for each curve.

Figure 3 shows plots of both I_Σ and $I_{\delta+\eta}$ obtained for ethanol, NH_3 and H_2O using an ESEM at gas pressures of (a) 0.5, (b) 1 and (c) 5 Torr, respectively. Each curve is plotted

6

up to the voltage which marks the onset of dielectric breakdown of the gas and hence the maximum useful amplification efficiency of the gas. Ethanol is able to sustain the highest breakdown current I_Σ^{max} at all pressures, while $I_{\delta+\eta}^{max}$ is very similar to NH_3 and H_2O at 5 Torr.
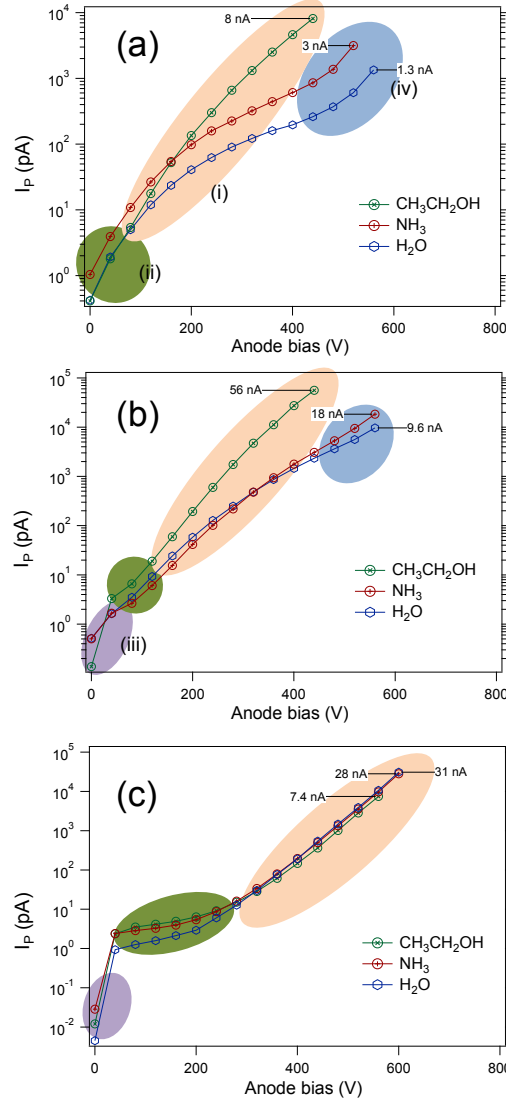

Figure 4: Gas-amplified photoelectron emission current (I_p) measured versus EPYS detector anode bias using ethanol, NH_3 and H_2O, at gas pressures of (a) 0.1 Torr, (b) 1 Torr, and (c) 5 Torr. The maximum current reached at the onset of dielectric breakdown of the gas is shown for each curve. The three amplification regimes (i, ii, iii and iv) labelled on the plots are discussed in the main text.

Figure 4 shows plots of I_p obtained for ethanol, NH_3 and H_2O using our EPYS system at gas pressures of (a) 0.5, (b) 1 and (c) 5 Torr, respectively. The values of I_p were collected

7

in 40 V increments until breakdown occurred.

Our results show that ethanol is a more efficient gas amplification medium than NH_3 and H_2O at gas pressures lower than ~ 5 Torr, and comparable at 5 Torr. In order to explain the amplification properties of the three gases, we must consider electron energy loss and gain mechanisms in the gas cascade.

The rate of change of energy of an electron in the gas cascade ($\partial E/\partial s$, where s is the electron trajectory between the sample and the detector anode) has three primary components:

$$\frac{\partial E}{\partial s} = \Gamma - \Omega - \Lambda \tag{1}$$

where:

- Γ is the rate at which electrons gain energy under the influence of the electric field between the sample and the detector anode.

- Ω is the rate at which energy is lost through ionizing collisions that increase the cascade current. It is determined by the inelastic cross-sections for electron-gas scattering processes that lead to ionization.

- Λ is the rate at which energy is lost via non-ionizing inelastic scattering events. It is determined by the inelastic cross-sections for scattering processes that do not lead to ionization (e.g. those corresponding to vibrational and rotation modes of gas molecules[34]).

Dependence of amplification on pressure

In Figure 2, gas amplification of electrons increases with pressure, reaches a maximum, then begins to decrease for each gas. The rate of increase is governed by Ω which is greatest for ethanol, followed by NH_3 and lowest for H_2O. The rate of decrease is governed primarily by Λ, which is also greatest for ethanol, followed by NH_3 and H_2O. The relative values of Ω and Λ determine the critical pressure at which the amplification efficiency is greatest for each gas.

The general shape of the curves in Figure 2 is well understood.[26,27,33] At very low pressures, amplification is low because the electron mean free path is long, the number of electron-molecule collisions in the gas is small, and amplification increases with pressure as the number density of gas molecules increases. However, the increase in the collision rate with pressure causes a decrease in the mean electron energy, and a decrease in the amount of energy gained by electrons between collisions. This trend eventually causes amplification to decrease with increasing pressure because non-ionizing collisions dominate at low electron energies, particularly below the ionization threshold (E_0) of the gas.[34] Thus, $1/E_0$ typically correlates with amplification efficiency,[27] and E_0 is often used as a figure of merit for the relative amplification efficiency of a given gas. However, ethanol, NH_3 and H_2O have ionization thresholds of 10.5, 10.1 and 12.6 eV respectively,[35–37] which cannot be used to explain why ethanol is a more efficient amplifier than NH_3 and H_2O. This can, however, be explained by the valence orbital structures of the gas molecules, and in particular the number of outer shell electrons with a binding energy that is similar to E_0, illustrated by the Lewis structures shown in Fig 1 (d). The contribution of valence orbitals to interaction cross-sections is described by a basic additivity rule,[38,39] which builds a total cross section of a molecule by summing the number of valence electrons (and nuclei) of the constituent atoms. Modified additivity rules have been developed to account for molecular geometries and the redistribution of atomic electrons due to molecular binding.[40,41] However, as a general rule molecules composed of a greater number of atoms have larger scattering cross sections,[42,43] thus they posses a relatively large Ω for high electron energies. The ionization energy and number of valence electrons for ethanol, NH_3 and H_2O are summarized in Table 1.

Table 1: Ionization energy and the number of valence electrons of the gaseous molecules H_2O, NH_3 and CH_3CH_2OH.

Molecule	Ionization energy (eV)	Number of valence electrons
H_2O	12.3	8
NH_3	10.1	8
CH_3CH_2OH	10.5	20

Dependence of amplification on detector bias

The plots in Figure 4 demonstrate a benefit of using EPYS to characterize the gas cascade. The emitted photoelectrons have a narrow energy distribution concentrated below the ionization threshold of each gas. All electrons must therefore be accelerated beyond E_0 before they can contribute to the gas cascade, and subtle variations in amplification behavior are therefore resolved as changes in how I_p scales with anode bias. Four distinct scaling regimes, labeled (i)-(iv), are resolved and indicated on the plots (we note that at low anode biases, when $I_p < 30$ pA, absolute differences between the curves should be ignored since they are on the order of variations in the direct current offset of each dataset).

In regime (i) gas cascade amplification scales approximately exponentially with anode bias. Exponential scaling is expected from the ideal Townsend gas capacitor model[44] (ie: a straight line, as seen on the logarithmic plot in Figure 4c). It is observed under conditions of high pressure and high anode bias, where the electron energy distribution is in a steady state throughout the vast majority of the sample-anode gap (ie: $\Gamma = \Omega + \Lambda$) shown in Figure 1c. In this gas amplification regime, the system is in the so-called 'swarm-condition'.[26] At reduced pressures (Figure 4a-b), the scaling in regime (i) is not exponential because $\Gamma \neq \Omega + \Lambda$, and changes in anode bias alter the energy distribution of electrons in the gas.

At low voltages, regime (ii), electron-ion recombination in the gas is significant and the scaling of I_p with bias is modified by the effects of the voltage on the recombination/separation efficiency. At very low voltages and high pressures, regime (iii), some electrons are never accelerated beyond E_0, and a subtle increase in bias can cause an abrupt increase in amplification (Figure 4c).

At high voltages and low pressures (iv), super-exponential scaling is observed in some cases, just before the onset of breakdown. This is attributed to an amplification feedback effect that is discussed below. The super-exponential scaling is observed when amplification is relatively low, and changes slowly as the voltage is increased. When the amplification factor is large (and increasing quickly with bias) and the feedback coefficient is low, the contribution

to I_Σ from feedback rises very quickly over a small voltage range close to breakdown, and is not resolved in the curves in Figure 4.

Ultimate amplification efficiency and dielectric breakdown

Ultimate amplification efficiency is limited by dielectric breakdown of the gas, which is governed by a positive feedback coefficient (k). The coefficient is non-zero due to electron ejection from the sample caused by positive ions and excited neutral gas molecules that are generated in the gas cascade and come into contact with the sample surface. The ejected electrons are normally attributed to potential rather than kinetic energy transfer from the ions and excited neutrals to the sample surface. Hence, the emitted electrons are typically believed to be Auger electrons and photoelectrons induced by ions and excited gas molecules that neutralize and de-excite at the sample surface.[26,44] In this framework, large, complex molecules have small feedback coefficients because they possess a large number of vibrational and rotational modes through which they can dissipate energy as they neutralize/de-excite at a surface.[44] This is consistent with the observation that ethanol exhibits the largest maximum breakdown current, followed by NH_3 and H_2O, under most conditions investigated in the present work (see Figures 3 and 4).

Conclusion

We have identified ethanol as a very efficient amplification gas compared to NH_3 and H_2O in both ESEM and EPYS. Both techniques were used to characterize the gas amplification properties of each gas. The rates of electron energy loss due to ionizing (Λ) and non-ionizing (Ω) inelastic scattering events are attributed to the valence orbital structure and molecular complexity. EPYS was used to study the anode bias dependence of amplification and four regimes were identified. These include standard Townsend amplification, super-exponential scaling arising from feedback at high biases, the effect of low bias on separation/recombination of

low energy electrons and small changes in bias shifting the median electron energy above the gas ionization threshold.

Acknowledgements

References

(1) Danilatos, G. Foundations of Environmental Scanning Electron Microscopy. *Adv. Electron. Electron Phys.* **1988**, *71*, 109–250.

(2) Moncrieff, D. A.; Robinson, V. N. E.; Harris, L. B. Charge Neutralization Of Insulating Surfaces In The SEM by Gas Ionization. *J. Phys. D* **1978**, *11*, 2315–2325.

(3) Thiel, B. L.; Toth, M. Secondary Electron Contrast in Low-Vacuum/Environmental Scanning Electron Microscopy of Dielectrics. *J. Appl. Phys.* **2005**, *97*, 051101.

(4) Yamada, Y.; Ikuta, T.; Nishiyama, T.; Takahashi, K.; Takata, Y. Droplet Nucleation on a Well-Defined Hydrophilic-Hydrophobic Surface of 10 nm Order Resolution. *Langmuir* **2014**, *30*, 14532–14537.

(5) Miljkovic, N.; Enright, R.; Wang, E. N. Effect of Droplet Morphology on Growth Dynamics and Heat Transfer During Condensation on Superhydrophobic Nanostructured Surfaces. *ACS Nano* **2012**, *6*, 1776–1785.

(6) Amadei, C. A.; Lai, C. Y.; Esplandiu, M. J.; Alzina, F.; Vecitis, C. D.; Verdaguer, A.; Chiesa, M. Elucidation of the Wettability of Graphene Through a Multi-Length-Scale Investigation Approach. *RSC Adv.* **2015**, *5*, 39532–39538.

(7) Rykaczewski, K. Microdroplet Growth Mechanism During Water Condensation on Superhydrophobic Surfaces. *Langmuir* **2012**, *28*, 7720–7729.

(8) Li, G.; Alhosani, M. H.; Yuan, S.; Liu, H.; Al Ghaferi, A.; Zhang, T. Microscopic Droplet Formation and Energy Transport Analysis of Condensation on Scalable Superhydrophobic Nanostructured Copper Oxide Surfaces. *Langmuir* **2014**, *30*, 14498–14511.

(9) Rykaczewski, K.; Chinn, J.; Walker, M. L.; Scott, J. H. J.; Chinn, A.; Jones, W. Dynamics of Nanoparticle Self-Assembly into Superhydrophobic Liquid Marbles During Water Condensation. *ACS nano* **2011**, *5*, 9746–9754.

(10) Carrier, B.; Wang, L.; Vandamme, M.; Pellenq, R. J. M.; Bornert, M.; Tanguy, A.; Van Damme, H. ESEM Study of the Humidity-Induced Swelling of Clay Film. *Langmuir* **2013**, *29*, 12823–12833.

(11) Rossi, M. P.; Ye, H. H.; Gogotsi, Y.; Babu, S.; Ndungu, P.; Bradley, J. C. Environmental Scanning Electron Microscopy Study of Water in Carbon Nanopipes. *Nano Lett.* **2004**, *4*, 989–993.

(12) Kolíbal, M.; Novák, L.; Shanley, T.; Toth, M.; Šikola, T. Silicon Oxide Nanowire Growth Mechanisms Revealed by Real-Time Electron Microscopy. *Nanoscale* **2016**, *8*, 266–275.

(13) Randolph, S. J.; Botman, A.; Toth, M. Capsule-Free Fluid Delivery and Beam-Induced Electrodeposition in a Scanning Electron Microscope. *RSC Adv.* **2013**, *3*, 20016–20032.

(14) Bresin, M.; Botman, A.; Randolph, S.; Straw, M.; Hastings, J. Liquid Phase Electron-Beam-Induced Deposition on Bulk Substrates using Environmental Scanning Electron Microscopy. *Microsc. Microanal.* **2014**, *20*, 376–384.

(15) Perry, J. M.; Harms, Z. D.; Jacobson, S. C. 3D Nanofluidic Channels Shaped by Electron-Beam-Induced Etching. *Small* **2012**, *8*, 1521–1526.

(16) Toth, M.; Lobo, C.; Knowles, W.; Phillips, M.; Postek, M.; Vladár, A. Nanostructure Fabrication by Ultra-High-Resolution Environmental Scanning Electron Microscopy. *Nano Lett.* **2007**, *7*, 525–530.

(17) Martin, A. A.; Bahm, A.; Bishop, J.; Aharonovich, I.; Toth, M. Dynamic Pattern Formation in Electron-Beam-Induced Etching. *Phys. Rev. Lett.* **2015**, *115*, 255501.

(18) Martin, A. A.; Toth, M.; Aharonovich, I. Subtractive 3D Printing of Optically Active Diamond Structures. *Sci. Rep.* **2014**, *4*, 5022.

(19) Niitsuma, J.; Yuan, X.; Koizumi, S.; Sekiguchi, T. Nanoprocessing of Diamond Using a Variable Pressure Scanning Electron Microscope. *Jpn. J. Appl. Phys.* **2006**, *45*, L71–L73.

(20) Fletcher, A.; Thiel, B.; Donald, A. Amplification Measurements of Alternative Imaging Gases in Environmental SEM. *J. Phys. D* **1997**, *30*, 2249–2257.

(21) Lobo, C. J.; Martin, A.; Phillips, M. R.; Toth, M. Electron Beam Induced Chemical Dry Etching and Imaging in Gaseous NH_3 Environments. *Nanotechnology* **2012**, *23*, 375302.

(22) Honda, M.; Kanai, K.; Komatsu, K.; Ouchi, Y.; Ishii, H.; Seki, K. Atmospheric Effect on the Ionization Energy of Titanyl Phthalocyanine Thin Film as Studied by Photoemission Yield Spectroscopy. *Mol. Cryst. Liq. Cryst.* **2006**, *455*, 219–225.

(23) Honda, M.; Kanai, K.; Komatsu, K.; Ouchi, Y.; Ishii, H.; Seki, K. Atmospheric Effect of Air, N_2, O_2, and Water Vapor on the Ionization Energy of Titanyl Phthalocyanine Thin Film Studied by Photoemission Yield Spectroscopy. *J. Appl. Phys.* **2007**, *102*, 103704.

(24) Nakayama, Y.; MacHida, S.; Minari, T.; Tsukagishi, K.; Noguchi, Y.; Ishii, H. Direct

Observation of the Electronic States of Single Crystalline Rubrene Under Ambient Condition by Photoelectron Yield Spectroscopy. *Appl. Phys. Lett.* **2008**, *93*, 173305.

(25) Shanley, T. W.; Martin, A. A.; Aharonovich, I.; Toth, M. Localized Chemical Switching of the Charge State of Nitrogen-Vacancy Luminescence Centers in Diamond. *Appl. Phys. Lett.* **2014**, *105*, 063103.

(26) Thiel, B.; Bache, I.; Fletcher, A.; Meredith, P.; Donald, A. An Improved Model for Gaseous Amplification in the Environmental SEM. *J. Microsc.* **1997**, *187*, 143–157.

(27) Thiel, B. L. Master Murves for Gas Amplification in Low Vacuum and Environmental Scanning Electron Microscopy. *Ultramicroscopy* **2004**, *99*, 35–47.

(28) Joy, D. C.; Joy, C. S. Low Voltage Scanning Electron Microscopy. *Micron* **1996**, *27*, 247–263.

(29) Toth, M.; Knowles, W. R.; Thiel, B. L. Secondary Electron Imaging of Nonconductors with Nanometer Resolution. *Appl. Phys. Lett.* **2006**, *88*, 023105.

(30) Kucheyev, S. O.; Toth, M.; Baumann, T. F.; Hamza, A. V.; Ilavsky, J.; Knowles, W. R.; Saw, C. K.; Thiel, B. L.; Tileli, V.; van Buuren, T.; Wang, Y. M.; Willey, T. M. Structure of Low-Density Nanoporous Dielectrics Revealed by Low-Vacuum Electron Microscopy and Small-Angle X-Ray Scattering. *Langmuir* **2007**, *23*, 353–356.

(31) Stokes, D. J.; Thiel, B. L.; Donald, A. M. Direct Observation of Water-Oil Emulsion Systems in the Liquid State by Environmental Scanning Electron Microscopy. *Langmuir* **1998**, *14*, 4402–4408.

(32) Toth, M.; Kucheyev, S. O.; Williams, J. S.; Jagadish, C.; Phillips, M. R.; Li, G. Imaging Charge Trap Distributions in GaN Using Environmental Scanning Electron Mcroscopy. *Appl. Phys. Lett.* **2000**, *77*, 1342–1344.

(33) Meredith, P.; Donald, A. M.; Thiel, B. Electron-Gas Interactions in the Environmental Scanning Electron Microscopes Gaseous Detector. *Scanning* **1996**, *18*, 467–473.

(34) Itikawa, Y.; Mason, N. Cross Sections for Electron Collisions with Water Molecules. *J. Phys. Chem. Ref. Data* **2005**, *34*, 1–22.

(35) Locht, R.; Leyh, B.; Denzer, W.; Hagenow, G.; Baumgärtel, H. The Photoionization of Ammonia Revisited. The Vibrational Autoionization of NH_3 and its three isotopomers in the 10–12 eV photon energy range. *Chem. Phys.* **1991**, *155*, 407–422.

(36) Snow, K. B.; Thomas, T. F. Mass Spectrum, Ionization Potentials and Appearance Potentials for Fragment Ions of Sulfuric Acid Vapor. *Int. J. Mass Spectrom. Ion Processes* **1990**, *96*, 49–68.

(37) Bowen, R. D.; Maccoll, A. Low Energy, Low Temperature Mass Spectra 2—Low Energy, Low Temperature Mass Spectra of Some Small Saturated Alcohols and Ethers. *Org. Mass Spectrom.* **1984**, *19*, 379–384.

(38) Jiang, Y.; Sun, J.; Wan, L. Additivity Rule for the Calculation of Electron Scattering from Polyatomic Molecules. *Phys. Rev. A* **2000**, *62*, 062712.

(39) Deutsch, H.; Cornelissen, C.; Cespiva, L.; Bonacic-Koutecky, V.; Margreiter, D.; Märk, T. D. Total Electron Impact Ionization Cross Sections of Free Molecular Radicals: the Failure of the Additivity Rule Revisited. *Int. J. Mass Spectrom. Ion Processes* **1993**, *129*, 43–48.

(40) Deutsch, H.; Becker, K.; Basner, R.; Schmidt, M.; Märk, T. D. Application of the Modified Additivity Rule to the Calculation of Electron-Impact Ionization Cross Sections of Complex Molecules. *J. Phys. Chem. A* **1998**, *102*, 8819–8826.

(41) Watson, R. L.; Peng, Y.; Horvat, V.; Kim, G. J.; Olson, R. E. Target Z Dependence

and Additivity of Cross Sections for Electron Loss by 6-MeV/amu Xe18$^+$ Projectiles . *Phys. Rev. A* **2003**, *67*, 022706.

(42) Margreiter, D.; Schmidt, M. Electron Impact Ionization Cross Sections of Molecules: Part II. Theoretical Determination of Total (counting) Ionization Cross Sections of Molecules: a New Approach. *Int. J. Mass Spectrom. Ion Processes* **1990**, *100*, 157–176.

(43) Hwang, W.; Kim, Y. K.; Rudd, M. E. New Model for Electron-Impact Ionization Cross Sections of Molecules. *J. Chem. Phys.* **1996**, *104*, 2956–2966.

(44) Von Engel, A. *Ionized Gases*; American Inst. of Physics, 1997.

Graphical TOC Entry